

Cluster detection in weak lensing surveys

F. Feroz^{1*}, P.J. Marshall² and M.P. Hobson¹

¹*Astrophysics Group, Cavendish Laboratory, JJ Thomson Avenue, Cambridge CB3 0HE, UK*

²*UC Santa Barbara, Santa Barbara CA 93106, USA*

Accepted —. Received —; in original form 30 October 2018

ABSTRACT

We present an efficient and robust approach for extracting clusters of galaxies from weak lensing survey data and measuring their properties. We use simple, physically-motivated cluster models appropriate for such sparse, noisy data, and incorporate our knowledge of the cluster mass function to optimise the detection of low-mass objects. Despite the method’s non-linear nature, we are able to search at a rate of approximately half a square degree per hour on a single processor, making this technique a viable candidate for future wide-field surveys. We quantify, for two simulated data-sets, the accuracy of recovered cluster parameters, and discuss the completeness and purity of our shear-selected cluster catalogues.

Key words: methods: data analysis – methods: statistical – cosmology:observations – galaxies: clusters: general

1 INTRODUCTION

Clusters of galaxies are the most massive gravitationally bound objects in the universe and, as such, are critical tracers of the formation of large-scale structure. The number count of clusters as a function of their mass and redshift has been predicted both analytically (see e.g. Press & Schechter 1974; Sheth et al. 2001) and from large scale numerical simulations (see e.g. Jenkins et al. 2001; Evrard et al. 2002), and are particularly sensitive to the cosmological parameters σ_8 and Ω_m (see e.g. Battye & Weller 2003). The size and formation history of massive clusters is such that the ratio of gas mass to total mass is expected to be representative of the universal ratio Ω_b/Ω_m , once the relatively small amount of baryonic matter in the cluster galaxies is taken into account (see e.g. White et al. 1993).

The study of cosmic shear has rapidly progressed with the availability of high quality wide-field lensing data. Large dedicated surveys with ground-based telescopes have been employed to reconstruct the mass distribution of the universe and constrain cosmological parameters (see e.g. Massey et al. 2007, 2005; Hoekstra et al. 2006). Weak lensing also allows one to detect galaxy clusters without making any assumptions about the baryon fraction, richness, morphology or dynamical state of the cluster, and so weak lensing cluster modelling would allow one to test these assumptions by observing the cluster with optical, X-ray or Sunyaev-Zel’dovich (SZ) methods.

Despite the advances in data quality, weak lensing data remains very sparse and noisy. Hence, obtaining the shear signal from the shapes of the background galaxies is a very challenging task. Several grid-based methods have been devised to reconstruct the

projected mass distribution from the observed shear field (see e.g. Kaiser & Squires 1993; Squires & Kaiser 1996; Bridle et al. 1999; Starck et al. 2006). In these “non-parametric” methods, the model assumed is a grid of pixels whose values comprise the model parameters. Marshall et al. (2002) showed that such a large number of parameters is often not justified by the data quality – failure to recognise this can result in over-fitting and over-interpretation of the data.

An alternative method for mass reconstruction is to work with simply-parameterised physically-motivated models for the underlying mass distribution (Marshall et al. 2003). By fitting simple template cluster models to the observed data set, we can draw inferences about the cluster parameters directly. This involves calculating the probability distribution of these parameters, and also (perhaps) those of the background cosmology; we can also compare different cluster models, enhancing our astrophysical understanding of these systems. This is most conveniently done through a Bayesian inference.

In Marshall et al. (2003) and Marshall (2006) a Bayesian approach was presented for such an analysis of weak lensing data from pointed observations towards known clusters. This used a highly effective, but computationally intensive, Markov Chain Monte Carlo (MCMC) sampler to explore the high-dimensional parameter space, and employed the thermodynamic integration technique to calculate the Bayesian evidence. In this paper, we extend this work by utilizing the recently developed ‘multimodal nested sampling’ (MULTINEST) technique (Feroz & Hobson 2008; Feroz et al. 2008), which is found to be ~ 200 times more efficient than traditional MCMC methods and thus enables one to search for multiple clusters in wide-field weak lensing data. MULTINEST enables one to simultaneously detect clusters from the weak lensing data and perform the parameter estimation for the individual cluster

* E-mail: f.feroz@mrao.cam.ac.uk

model parameters. Furthermore, following Hobson & McLachlan (2003), we also quantify our cluster detection through the application of Bayesian model selection using the Bayesian evidence value for each detected cluster, which can be easily calculated using the MULTINEST technique.

The outline of this paper is as follows. In Section 2 we describe our methodology for detecting and characterising clusters in weak lensing survey data. In Section 3 we apply our method to a simple simulated data-set, before moving on to describe realistic cluster survey simulations and the results of our cluster extraction algorithm on these simulations in Section 4. Finally we present our conclusions in Section 5.

2 METHODOLOGY

2.1 Bayesian inference

Our cluster detection methodology is built upon the principles of Bayesian inference, and so we begin by giving a brief summary of this framework. Bayesian inference methods provide a consistent approach to the estimation of a set of parameters Θ in a model (or hypothesis) H for the data \mathbf{D} . Bayes' theorem states that

$$\Pr(\Theta|\mathbf{D}, H) = \frac{\Pr(\mathbf{D}|\Theta, H) \Pr(\Theta|H)}{\Pr(\mathbf{D}|H)}, \quad (1)$$

where $\Pr(\Theta|\mathbf{D}, H) \equiv P(\Theta)$ is the posterior probability distribution of the parameters, $\Pr(\mathbf{D}|\Theta, H) \equiv \mathcal{L}(\Theta)$ is the likelihood, $\Pr(\Theta|H) \equiv \pi(\Theta)$ is the prior, and $\Pr(\mathbf{D}|H) \equiv \mathcal{Z}$ is the Bayesian evidence.

In parameter estimation, the normalising evidence factor is usually ignored, since it is independent of the parameters Θ , and inferences are obtained by taking samples from the (unnormalised) posterior using standard MCMC sampling methods, where at equilibrium the chain contains a set of samples from the parameter space distributed according to the posterior. This posterior constitutes the complete Bayesian inference of the parameter values, and can be marginalised over each parameter to obtain individual parameter constraints.

In contrast to parameter estimation problems, for model selection the evidence takes the central role and is simply the factor required to normalize the posterior over Θ :

$$\mathcal{Z} = \int \mathcal{L}(\Theta) \pi(\Theta) d^D \Theta, \quad (2)$$

where D is the dimensionality of the parameter space. As the average of the likelihood over the prior, the evidence is larger for a model if more of its parameter space is likely and smaller for a model with large areas in its parameter space having low likelihood values, even if the likelihood function is very highly peaked. Thus, the evidence automatically implements Occam's razor: a simpler theory with compact parameter space will have a larger evidence than a more complicated one, unless the latter is significantly better at explaining the data. The question of model selection between two models H_0 and H_1 can then be decided by comparing their respective posterior probabilities given the observed data set \mathbf{D} , as follows

$$R = \frac{\Pr(H_1|\mathbf{D})}{\Pr(H_0|\mathbf{D})} = \frac{\Pr(\mathbf{D}|H_1) \Pr(H_1)}{\Pr(\mathbf{D}|H_0) \Pr(H_0)} = \frac{\mathcal{Z}_1 \Pr(H_1)}{\mathcal{Z}_0 \Pr(H_0)}, \quad (3)$$

where $\Pr(H_1)/\Pr(H_0)$ is the a priori probability ratio for the two models, which can often be set to unity but occasionally requires further consideration.

Evaluation of the multidimensional integral in Eq. 2 is a challenging numerical task. Standard techniques like thermodynamic integration are extremely computationally expensive which makes evidence evaluation at least an order of magnitude more costly than parameter estimation. Some fast approximate methods have been used for evidence evaluation, such as treating the posterior as a multivariate Gaussian centred at its peak (see e.g. Hobson & McLachlan 2003), but this approximation is clearly a poor one for multimodal posteriors (except perhaps if one performs a separate Gaussian approximation at each mode). The Savage-Dickey density ratio has also been proposed (see e.g. Trotta 2007) as an exact, and potentially faster, means of evaluating evidences, but is restricted to the special case of nested hypotheses and a separable prior on the model parameters. Various alternative information criteria for astrophysical model selection are discussed by Liddle (2007), but the evidence remains the preferred method.

The nested sampling approach, introduced by Skilling (2004), is a Monte Carlo method targeted at the efficient calculation of the evidence, but also produces posterior inferences as a by-product. Feroz & Hobson (2008) and Feroz et al. (2008) built on this nested sampling framework and have recently introduced the MULTINEST algorithm which is very efficient in sampling from posteriors that may contain multiple modes and/or large (curving) degeneracies and also calculates the evidence. This technique has greatly reduced the computational cost of Bayesian parameter estimation and model selection, and is employed in this paper.

2.2 Weak lensing likelihood

Our approach to detecting multiple clusters in weak lensing data follows the generic object detection strategy advocated by Hobson & McLachlan (2003) and refined by Feroz & Hobson (2008). They show that the straightforward approach of using a single-object model for the data is both computationally far less demanding than adopting a multiple-object model and reliable, provided that the objects of interest are spatially well-separated. It is important to understand that adopting a single-object model does *not* restrict one to detecting just a single cluster in the weak lensing data. Rather, by modelling the data in this way, one expects the posterior distribution to possess local maxima in the parameter space Θ of the single-cluster model, some of which will correspond to real clusters present in the data and some that occur because the pattern of ellipticities in the background galaxies 'conspire' to give the impression that a cluster might be present. The process of object detection and characterisation thus reduces to locating the local maxima of the posterior distribution in the parameter space Θ and deciding which of these local maxima correspond to a real cluster.

A model cluster density profile can be determined from numerical N -body simulations of large-scale structure formation in a Λ CDM universe. In particular, assuming spherical symmetry, the NFW profile (Navarro et al. 1997) provides a good fit to the simulations and is given by

$$\rho(r) = \frac{\rho_s}{(r/r_s)(1+r/r_s)^2}, \quad (4)$$

where r_s and ρ_s are the radius and density at which the logarithmic slope breaks from -1 to -3 . The mass M_{200} contained within the radius r_{200} at which the density is 200 times the cosmological critical density ρ_{crit} at the redshift of the cluster can be calculated as

(Evrard et al. 2002; Allen et al. 2003):

$$\begin{aligned} \frac{M_{200}}{(4/3)\pi r_{200}^3} &= 200\rho_{\text{crit}}, \\ &= 4\pi\rho_s r_s^3 \left[\log(1+c) - \frac{c}{1+c} \right], \end{aligned} \quad (5)$$

where $c = r_{200}/r_s$ is a measure of the halo concentration. Thus, we take as our cluster parameters $\Theta = (x_c, y_c, M_{200}, c, z)$, where x_c and y_c are the spatial coordinates at which the cluster is centred, and z is its redshift.

A cluster mass distribution is investigated using weak gravitational lensing through the relationship (see e.g. Schramm & Kayser 1995):

$$\langle \epsilon(\mathbf{x}) \rangle = g(\mathbf{x}), \quad (6)$$

that is, at any point \mathbf{x} on the sky, the local average of the complex ellipticities $\epsilon = \epsilon_1 + i\epsilon_2$ of a collection of background galaxy images is an unbiased estimator of the local complex reduced shear field, $g = g_1 + ig_2$, due to the cluster. Adopting the thin-lens approximation, for a projected mass distribution $\Sigma(\mathbf{x})$ in the lens, the reduced shear $g(\mathbf{x})$ is defined as

$$g(\mathbf{x}) = \frac{\gamma(\mathbf{x})}{1 - \kappa(\mathbf{x})}, \quad (7)$$

where the convergence $\kappa(\mathbf{x})$ is given by

$$\kappa(\mathbf{x}) = \frac{\Sigma(\mathbf{x})}{\Sigma_{\text{crit}}} \quad (8)$$

and the shear $\gamma(\mathbf{x})$ can, in general, be written as a convolution integral over the convergence $\kappa(\mathbf{x})$ (see e.g. Bridle et al. 1999). Σ_{crit} is the critical surface mass density

$$\Sigma_{\text{crit}} = \frac{c^2}{4\pi G} \frac{D_s}{D_1 D_{1s}}. \quad (9)$$

where D_s , D_1 and D_{1s} are the angular-diameter distances between, respectively, the observer and each galaxy, the observer and the lens, and the lens and each galaxy. In general, the redshifts of each background galaxy can be different, but are assumed to be known. The lensing effect is said to be weak or strong if $\kappa \ll 1$ or $\kappa \gtrsim 1$ respectively. Analytic formulae for the convergence and shear fields produced by a cluster with an NFW profile have been calculated by Bartelmann (1996); Wright & Brainerd (2000); Meneghetti et al. (2003) and we make use of these here to reduce computational costs.

The observed complex ellipticity components of the N_{gal} background galaxies can be ordered into a data vector \mathbf{d} with components

$$\mathbf{d}_i = \begin{cases} \text{Re}(\epsilon_i) & (i \leq N_{\text{gal}}) \\ \text{Im}(\epsilon_{i-N_{\text{gal}}}) & (N_{\text{gal}} + 1 \leq i \leq 2N_{\text{gal}}) \end{cases}. \quad (10)$$

Likewise the corresponding components of the complex reduced shear $g(\mathbf{x}_i)$ at each galaxy position, as predicted by the cluster model, can be arranged into the predicted data vector \mathbf{d}^{P} , with the arrangement of components matching Eq. 10.

The uncertainty on the measured ellipticity components consists of two contributions. The intrinsic ellipticity components of the background galaxies (i.e. prior to lensing) may be taken as having been drawn independently from a Gaussian distribution with mean zero and variance σ_{int}^2 . Moreover, the effect of errors in the measured ellipticity components introduced by the galaxy shape estimation procedure can be modelled as Gaussian with mean zero

and variance σ_{obs}^2 . Assuming the intrinsic and observational contributions to the uncertainty are independent, one can simply add the two variances (see e.g. Hoekstra et al. 2000; Marshall et al. 2003). This leads to a diagonal noise covariance matrix \mathbf{C} on the ellipticity components, such that the elements corresponding to the i th galaxy are

$$\sigma_i^2 = \sigma_{\text{obs}}^2 + \sigma_{\text{int}}^2 [1 - \max(|g(\mathbf{x}_i)|^2, 1/|g(\mathbf{x}_i)|^2)]^2. \quad (11)$$

The term inside the square brackets is the correction for the galaxies lying very close to the critical regions of the strong lensing cluster as suggested by Schneider et al. (2000) and implemented by Bradač et al. (2004).

As shown by Marshall et al. (2003), we can then write the likelihood function as

$$\mathcal{L}(\Theta) = \frac{1}{Z_L} \exp(-\frac{1}{2}\chi^2), \quad (12)$$

where χ^2 is the usual misfit statistic

$$\chi^2 = (\mathbf{d} - \mathbf{d}^{\text{P}})^{\text{T}} \mathbf{C}^{-1} (\mathbf{d} - \mathbf{d}^{\text{P}}) \quad (13)$$

$$= \sum_{i=1}^{N_{\text{gal}}} \sum_{j=1}^2 \frac{(\epsilon_{j,i} - g_j(\mathbf{x}_i))^2}{\sigma_i^2}, \quad (14)$$

and the normalisation factor is

$$Z_L = (2\pi)^{2N_{\text{gal}}/2} |\mathbf{C}|^{1/2}. \quad (15)$$

Note that it is necessary to include this normalisation factor in the likelihood, since the covariance matrix \mathbf{C} is not constant, but depends on the cluster model parameters through the predicted shear terms in Eq. 11.

2.3 Priors on cluster parameters

To determine the model completely it only remains to specify the prior $\pi(\Theta)$ on the cluster parameters $\Theta = (x_c, y_c, M_{200}, c, z)$. Throughout this paper we assume the prior to be partly separable, such that

$$\pi(\Theta) = \pi(x_c)\pi(y_c)\pi(c)\pi(M_{200}, z). \quad (16)$$

We assume uniform priors on the position parameters x_c and y_c over ranges that slightly exceed the patch of sky for which lensing data is available, so that the model has the flexibility of having clusters that lie slightly outside the observed region. This is necessary since such clusters can still have measurable effects on the observed shear field. We also adopt the uniform prior $\pi(c) = \mathcal{U}(0, 15)$ on the cluster concentration parameter.

For the mass M_{200} (which we will denote henceforth by M for brevity) and redshift z parameters, we adopt a joint prior based on the Press-Schechter (Press & Schechter 1974) mass function within some ranges $M_{\text{min}} < M \leq M_{\text{max}}$ and $z_{\text{min}} < z \leq z_{\text{max}}$. The chosen minimum and maximum values of these ranges used in our analysis of simulated weak-lensing data are discussed below. Numerical simulations have shown that the Press-Schechter mass function over-estimates the abundance of high-mass clusters and under-estimates those of low mass (Sheth et al. 2001), but overall it still provides an adequate fit to N -body simulations (Jenkins et al. 2001). In particular, we assume the Press-Schechter mass function with $\sigma_8 = 0.8$, which is plotted in Figure 1, along with some samples drawn from it for illustration. In principle, one could allow σ_8 to be an additional free parameter in our model that we attempt to constrain simultaneously with the parameters describing individual

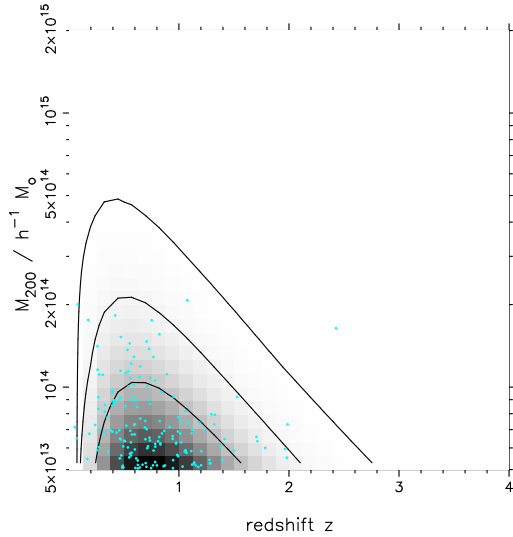


Figure 1. The Press-Schechter mass function with $\sigma_8 = 0.8$, together with some samples drawn from it for illustration. The contours enclose 68%, 95% and 99% of the probability.

clusters. We have not pursued this possibility in this first application of our method, but it will be explored in a future work. It should also be remembered that our adoption of the Press-Schechter mass function as a prior still allows for the possibility of detecting clusters with masses and redshifts that lie outside the ranges favoured by this mass function, provided the data, through the likelihood function, are sufficiently conclusive. Finally, we note that it is trivial to replace the assumed Press-Schechter mass function in our analysis by any other mass function, if so desired.

2.4 Quantifying cluster detection

As mentioned above, one expects the posterior distribution $P(\Theta)$ in the parameter space of our single-cluster model to possess numerous local maxima, some corresponding to real clusters and some occurring because the pattern of ellipticities in the background galaxies ‘conspire’ to give the impression that a cluster might be present. We now discuss how one may calculate the probability that an identified local peak in the posterior corresponds to a real cluster (or set of clusters), thereby quantifying our cluster detection methodology.

This quantification is most naturally performed via a Bayesian model selection by evaluating the evidence associated with each local posterior peak for competing models for the data (see e.g. Hobson & McLachlan 2003). For each peak, it is convenient to consider the following hypotheses:

H_0 = ‘no cluster with $M > M_{\text{lim}}$ is centred in S ’,

H_1 = ‘at least one cluster with $M > M_{\text{lim}}$ is centred in S ’,

where S is taken to be a region just enclosing (to a good approximation) the posterior peak in the spatial subspace $\mathbf{x}_c = (x_c, y_c)$, and M_{lim} is a lower limiting mass of interest that we discuss in more detail below. It is straightforward to see that H_0 and H_1 are mutually exclusive and exhaustive hypotheses. The null hypotheses H_0 is, however, the union of two other mutually exclusive hypothesis,

i.e. $H_0 = H_2 \cup H_3$, where

H_2 = ‘at least one cluster with $0 < M \leq M_{\text{lim}}$ is centred in S ’,

H_3 = ‘no cluster is centred in S ’.

Note that H_3 is equivalent to considering clusters of zero mass. Moreover, if one choose $M_{\text{lim}} = 0$, then H_2 becomes an empty hypothesis and $H_0 = H_3$.

For each posterior peak, we must calculate the model selection ratio R given in Eq. 3 between the hypotheses H_0 and H_1 . Using Bayes’ theorem and the fact that $H_0 = H_2 \cup H_3$, with H_2 and H_3 being mutually exclusive, it is easy to show that R becomes

$$R = \frac{\mathcal{Z}_1}{\mathcal{Z}_2 \left[1 + \frac{\text{Pr}(H_3)}{\text{Pr}(H_2)} \right]^{-1} + \mathcal{Z}_3 \left[1 + \frac{\text{Pr}(H_2)}{\text{Pr}(H_3)} \right]^{-1}} \frac{\text{Pr}(H_1)}{\text{Pr}(H_0)}. \quad (17)$$

Note that for the special case $M_{\text{lim}} = 0$, for which $P(H_2) = 0$ and $H_0 = H_3$, the ratio R correctly reduces to the right-hand side of Eq. 3.

For each hypothesis H_i ($i = 1, 2, 3$), the evidence is given by

$$\mathcal{Z}_i = \int \mathcal{L}(\Theta) \pi_i(\Theta) d\Theta, \quad (18)$$

where

$$\pi_i(\Theta) = \pi_i(\mathbf{x}_c) \pi_i(c) \pi_i(M, z), \quad (19)$$

for $i = 1, 2, 3$ are priors that define the hypotheses. In particular, the priors on the position of the cluster centre may be taken in all cases to be uniform: $\pi_i(\mathbf{x}_c) = 1/|S|$ for all i , where $|S|$ is the area of the region S . Similarly, for all hypotheses, the prior on cluster concentration may be taken $\pi_i(c) = \mathcal{U}(0, 15)$. Differences between the priors for the hypotheses do, however, occur in the joint priors $\pi_i(M, z)$ on the cluster mass and redshift. For hypothesis H_1 , the prior is the appropriately normalised Press-Schechter mass function over the ranges $M_{\text{lim}} < M \leq M_{\text{max}}$ and $z_{\text{min}} < z \leq z_{\text{max}}$, and is zero otherwise.¹ For H_2 , the prior is the appropriately normalised Press-Schechter mass function over the ranges $0 < M \leq M_{\text{lim}}$ and $z_{\text{min}} < z \leq z_{\text{max}}$, and is zero otherwise. Finally, for H_3 , the prior is $\pi_3(M, z) = \delta(M) \pi_3(z)$, where $\delta(M)$ is the Dirac delta function centred on $M = 0$ and $\pi_3(z)$ can be any normalised distribution.

Assuming the above priors, the evidence for each hypothesis can be written

$$\mathcal{Z}_i(S) = \frac{1}{|S|} \int_S \bar{P}_i(\mathbf{x}_c) d^2 \mathbf{x}_c, \quad (20)$$

where we have defined the (unnormalised) two-dimensional marginal posterior

$$\bar{P}_i(\mathbf{x}_c) = \iint \mathcal{L}(\mathbf{x}_c, c, M, z) \pi_i(c) \pi_i(M, z) dc dM dz. \quad (21)$$

The evidences (Eq. 20) for $i = 1, 2$ are easily obtained using the MULTINEST algorithm, which automatically identifies local peaks in the posterior and evaluates the ‘local’ evidence associated with each peak (Feroz & Hobson 2008; Feroz et al. 2008). One minor subtlety is that, when analysing the weak-lensing survey data, the uniform prior on the spatial position \mathbf{x}_c for clusters extends over

¹ Recall that, in any case, the Press-Schechter prior is assumed to be zero outside the ranges $M_{\text{min}} < M \leq M_{\text{max}}$ and $z_{\text{min}} < z \leq z_{\text{max}}$, as mentioned in Section 2.3. Thus, even for non-zero M_{lim} , if $M_{\text{lim}} \leq M_{\text{min}}$, then H_2 becomes an empty hypothesis and $H_0 = H_3$.

a region Ω that slightly exceeds the full patch of sky for which lensing data is available, i.e. $\pi(\mathbf{x}_c) = 1/|\Omega|$, as discussed in Section 2.3). Thus, the local evidence returned by MULTINEST as associated with some posterior peak must be multiplied by $|\Omega|/|S|$ to obtain the corresponding evidence (Eq. 20). Finally, the evidence $\mathcal{Z}_3(S)$ can be calculated directly without the need for any sampling as

$$\mathcal{Z}_3(S) = \frac{1}{|S|} \int_S \mathcal{L}_0 d^2\mathbf{x}_c = \mathcal{L}_0, \quad (22)$$

since $\mathcal{L}_0 \equiv \mathcal{L}(\mathbf{x}_c, c, M = 0, z)$ is, in fact, independent of the cluster parameters c and z and the priors are normalised. Note that \mathcal{Z}_3 is, in fact, independent of S .

So far we have not addressed the prior ratios $\Pr(H_1)/\Pr(H_0)$ and $\Pr(H_2)/\Pr(H_3)$ in Eq. 17. For the sake of illustration and simplicity, let us assume that the clusters are randomly distributed in spatial position. This is not entirely correct due to clustering of the galaxy clusters on large scales. Nonetheless, the departure from a random distribution in small fields is not expected to be significant. First, consider the ratio $\Pr(H_1)/\Pr(H_0)$. If μ_S is the (in general non-integer) expected number of clusters with $M > M_{\text{lim}}$ centred in a region of size $|S|$, then the probability of there being N such clusters in the region is Poisson distributed:

$$\Pr(N|\mu_S) = \frac{e^{-\mu_S} \mu_S^N}{N!}. \quad (23)$$

Thus, bearing in mind the above definitions of H_0 and H_1 , we have

$$\frac{\Pr(H_1)}{\Pr(H_0)} = \exp(\mu_S) - 1 \approx \mu_S \text{ for } \mu_S \ll 1, \quad (24)$$

where μ_S is given in terms of the mass function by

$$\mu_S = |S| \int_{z_{\text{min}}}^{z_{\text{max}}} \int_{M_{\text{lim}}}^{M_{\text{max}}} \frac{dn}{dM dz} dM dz, \quad (25)$$

where $dn/dM dz$ is the distribution of the projected number density of clusters with masses between M and dM and redshift between z and dz per unit area.

Let us now consider the ratio $\Pr(H_2)/\Pr(H_3)$. Similarly, let us suppose that λ_S is the (in general non-integer) expected number of clusters with $0 < M < M_{\text{lim}}$ centered in a region of size $|S|$. Then by the same argument as above

$$\frac{\Pr(H_2)}{\Pr(H_3)} = \exp(\lambda_S) - 1 \approx \lambda_S \text{ for } \lambda_S \ll 1, \quad (26)$$

where λ_S is given in terms of the mass function by

$$\lambda_S = |S| \int_{z_{\text{min}}}^{z_{\text{max}}} \int_{M_{\text{min}}}^{M_{\text{lim}}} \frac{dn}{dM dz} dM dz. \quad (27)$$

We are thus able to calculate the model selection ratio R in Eq. 17 for each local posterior peak, which gives us the relative probability for obtaining a ‘true’ cluster detection (H_1) as opposed to a ‘false’ one (H_0). In particular, if the k th local posterior peak has a ratio R_k , then the probability that this is a ‘true’ cluster detection is

$$p_k = \frac{R_k}{1 + R_k}. \quad (28)$$

If we define a ‘threshold probability’ p_{th} , such that detections with $p_k \geq p_{\text{th}}$ are identified as candidate clusters, the expected number of false positives, $\langle n_{\text{FP}} \rangle$ can then be calculated as

$$\langle n_{\text{FP}} \rangle = \sum_{k=1, p_k \geq p_{\text{th}}}^K (1 - p_k), \quad (29)$$

where K is total number of detected posterior peaks. The expected ‘purity’ of the resulting cluster sample, defined as the fraction of the cluster candidates that are ‘true’, can be similarly calculated.

The choice of threshold probability p_{th} depends on the application. A lower value of p_{th} will obviously result in a lower purity but higher completeness, especially at the low-mass end where the lensing signal is particularly weak. In the presence of more information (e.g. the multi-band photometry) a lower purity but higher completeness might be preferable and hence, p_{th} should be set to a lower value in such cases. In the absence of any additional information for the chosen survey field, p_{th} can be chosen so that the expected purity is relatively higher. We set $p_{\text{th}} = 0.5$ in this work, where we assume no additional information on the weak lensing simulations under analysis. This choice of p_{th} ensures that all the detections with a higher probability of being ‘true’ than being ‘false’ are identified as candidate clusters. We discuss the impact of p_{th} on the completeness and purity of the shear selected cluster sample derived from simulated weak-lensing data in Section 3.

2.5 Estimation of individual cluster parameters

Once a local posterior peak has been detected and identified as a cluster candidate using the above method, the values of the parameters $\Theta = (\mathbf{x}_c, c, M, z)$ associated with that cluster are easily calculated using the MULTINEST algorithm. The algorithm identifies the samples associated with each posterior peak and allows one to draw posterior inferences using just these samples (Feroz & Hobson 2008; Feroz et al. 2008). Thus, for example, one can construct full one-dimensional marginalised posterior distributions for each cluster parameter, from which best-fit values and uncertainties are trivially obtained.

3 APPLICATION TO TOY WEAK-LENSING SIMULATIONS

3.1 Simple weak-lensing survey simulation

Before applying our methodology to weak-lensing data derived from full N -body simulations in Section 4, we first demonstrate its performance in the ideal case, where the clusters have been simulated using exactly the same model as the one we assume for the analysis. This is helpful in validating our approach.

We simulate ten spherically-symmetric clusters, each with an NFW density profile, distributed uniformly in a 2000×2000 arcsec² field, with cluster masses and redshifts drawn from the Press-Schechter mass function with $M > 5 \times 10^{13} h^{-1} M_{\odot}$ and $0 \leq z \leq 1$. We assume a Λ CDM cosmology with $\Omega_{\text{m}} = 0.3$, $\Omega_{\Lambda} = 0.7$, $\sigma_8 = 0.8$ and Hubble parameter $h = 0.7$. The concentration parameter c for each cluster was drawn from a uniform distribution $\mathcal{U}(0, 15)$. The true cluster parameters are listed in Table 1 and the resulting convergence map is shown in Figure 2 (left panel).

We consider the data only in the middle 1800×1800 arcsec² region of the simulation in order to allow the cluster centers to lie outside the region for which data is available. We down-sample the resulting convergence and shear maps on a 256×256 pixel grid and add Gaussian noise with standard deviation $\sigma_n = \sigma_{\epsilon} / \sqrt{n_g A}$, where n_g is average number of galaxies per arcmin² and A is the pixel area. We assume $\sigma_{\epsilon} \simeq 0.3$ and $n_g \simeq 100$ gal/arcmin² as

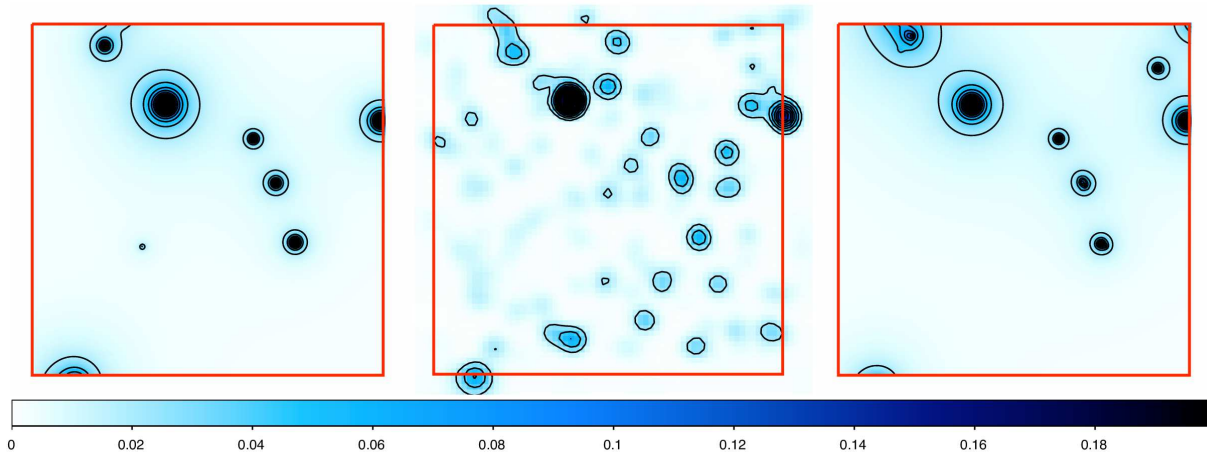


Figure 2. Left: true convergence map of the simulated clusters listed in Table 1. Middle: reconstructed convergence map obtained using the LenEnt2 algorithm. Right: inferred convergence map obtained using the MULTINEST algorithm.

	x/arcsec	y/arcsec	$M_{200}/h^{-1}M_{\odot}$	c	z
1	338.9	81.5	7.3×10^{13}	6.2	0.57
2	-691.2	-951.4	9.3×10^{13}	6.9	0.21
3	-539.1	785.3	5.9×10^{13}	4.0	0.50
4	-452.6	963.0	5.0×10^{13}	9.5	0.35
5	-345.6	-245.3	5.1×10^{13}	2.4	0.92
6	-757.1	-998.7	5.4×10^{13}	2.9	0.47
7	877.8	399.9	1.9×10^{14}	9.3	0.47
8	-266.5	483.2	3.2×10^{14}	9.4	0.37
9	223.6	308.4	5.3×10^{13}	11.1	0.57
10	437.9	-222.5	8.6×10^{13}	14.9	0.53

Table 1. True cluster parameters for the simple simulation discussed in Section 3.1.

is approximately found for space-based weak lensing surveys. We assume all the background galaxies to lie at redshift $z = 1$.

3.2 Analysis and results

We applied our cluster finding methodology, using the MULTINEST algorithm, to this simple weak lensing survey simulation. As mentioned in Section 2.3, we impose uniform priors on cluster positions with the range of the priors set to be slightly wider than the range for which the data is available. We also (correctly) impose a uniform prior $\mathcal{U}(0, 15)$ on the concentration parameter. For the mass and redshift, we apply a joint prior coming from the Press-Schechter mass function with $0 \leq z \leq 1$ and $5 \times 10^{13} \leq M/h^{-1}M_{\odot} \leq 5 \times 10^{15}$.

The MULTINEST algorithm identified 34 posterior peaks. For each peak, the probability that it corresponds to a real cluster was calculated as discussed in Section 2.4. M_{lim} was set to $5 \times 10^{15} h^{-1} M_{\odot}$. Adopting a threshold probability $p_{\text{th}} = 0.5$, 10 candidate clusters were identified. The corresponding inferred convergence map, made from the mean of 100 convergence maps with cluster parameter values drawn from their respective posterior distributions for the candidate clusters, is shown in the right-hand

panel of Figure 2. For comparison, in the centre panel we also show the convergence map reconstructed using the LenEnt2 algorithm (Marshall et al. 2003).

From Figure 2 one sees that 7 of the 10 candidate clusters correspond to real clusters. We must however, note that the two overlapping clusters 2 and 6 in Table 1, have been confused to yield a single detected cluster. Of the 10 candidate clusters, 3 were actually *false positives*, but we note that $R \sim 1$ for these clusters, corresponding to equal probability of these clusters being either true or spurious. The 2 real clusters that were not detected (clusters 4 and 5 in Table 1) are the least massive clusters in the simulation and consequently contribute a very small lensing signal. In fact, cluster 5 was detected by MULTINEST but had probability ratio $R < 1$, corresponding to the probability of it being ‘true’ of less than 0.5; consequently it was not identified as a candidate cluster with $p_{\text{th}} = 0.5$.

The inferred parameter values, with 68 per cent confidence limits, for each of the 32 detected posterior peaks are shown in Figure 3 (top panels). Also shown (bottom panels) is the $\log R$ value and mass M of each posterior peak. Figure 4 shows the values of the inferred parameters (in red) for peaks with $R > 1$, and hence identified as cluster candidates (with $p_{\text{th}} = 0.5$), together with the true parameter values (in blue) for the corresponding cluster.

In Figure 5, we also plot the expected and actual number of *false positives* obtained as a function of the ‘threshold probability’ p_{th} . The close agreement between the two curves indicates that our quantification procedure for cluster identification is extremely robust. The corresponding purity and completeness as a function of p_{th} are plotted in Figure 6.

Finally, we calculate the Receiver Operating Characteristic (ROC) curve (see e.g. Fawcett 2006) for our analysis procedure. The ROC curve provides a very reliable way of selecting the optimal algorithm in signal detection theory. We employ ROC curve here to analyse our cluster candidate identification criterion, based on the threshold probability p_{th} . The ROC curve plots the True Positive Rate (TPR) against the False Positive Rate (FPR) as a function of the threshold probability. TPR is the ratio of the number of *true positives* for a given p_{th} to the number of *true positives* in all the detected clusters (i.e. for $p_{\text{th}} = 0$) which for the present analysis

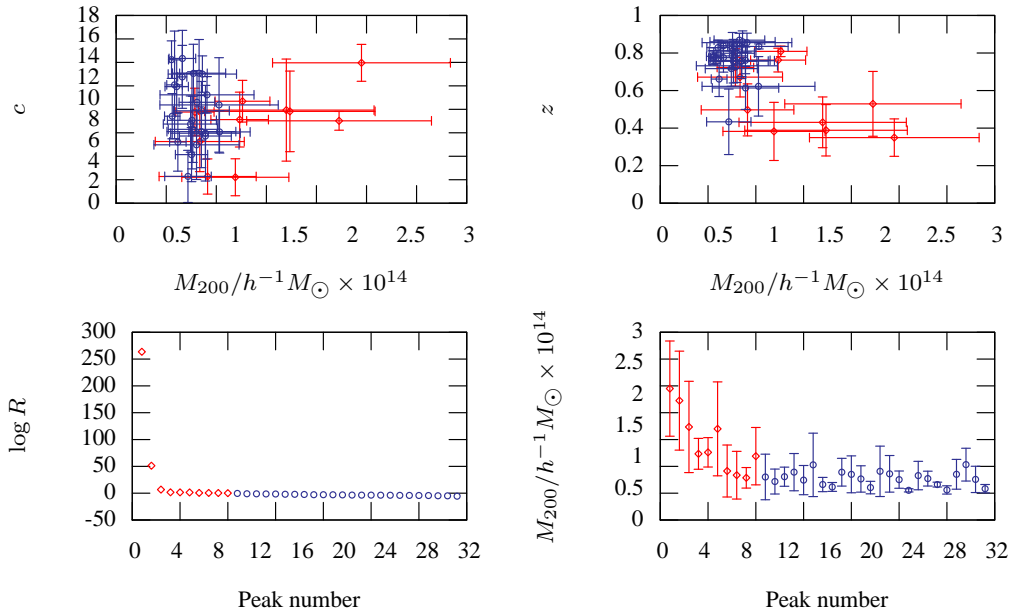


Figure 3. Top panels: inferred parameters values and 68 per cent confidence intervals for each of the posterior peaks detected by the MULTINEST algorithm when applied to the simple simulation discussed in Section 3.1. Bottom panels: the $\log R$ value and mass M of detected posterior peak. In both cases, peaks with $R > 1$ are plotted in red and the remaining peaks in blue.

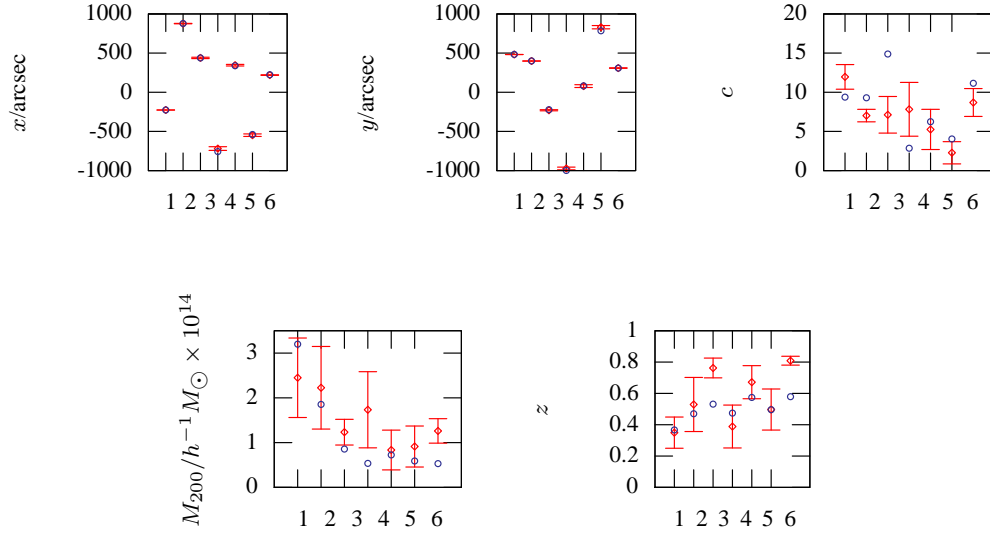


Figure 4. Inferred parameter values with 68 per cent confidence limits (red) compared to true parameter values (blue) for each candidate cluster.

is 8 corresponding to 8 clusters that had a strong enough lensing signal to be identified by our algorithm. Similarly, FPR is the ratio of the number of *false positives* for a given p_{th} to the number of *false positives* for $p_{\text{th}} = 0$. The best possible method would yield a point in the upper left corner of the ROC space, with coordinates (0,1). A completely random guess would, on average, yield a point on the diagonal line. The ROC curve traced out as a function of p_{th} for our cluster detection methodology is plotted in Figure 7. It can be seen that although, $p_{\text{th}} = 0.6$ gives the optimal cluster candi-

date identification criteria, $p_{\text{th}} = 0.5$ is very nearly as good. The accuracy of an algorithm can be measured by calculating the area under the ROC curve. An area of 1 represents a perfect algorithm while an area of 0.5 represents a worthless algorithm. We notice that the area under the ROC curve in Figure 7 is very close to 1.

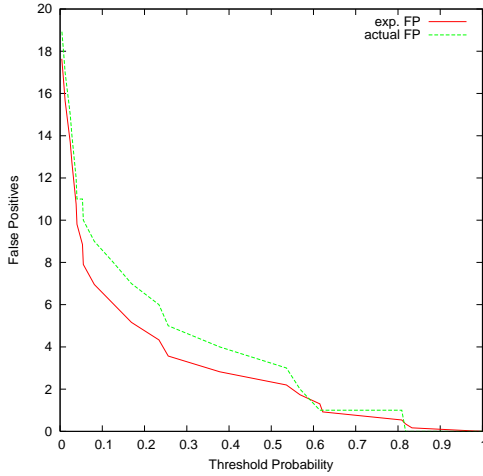


Figure 5. The expected and actual number of *false positives* as function of the ‘threshold probability’ p_{th} (see Section 2.4).

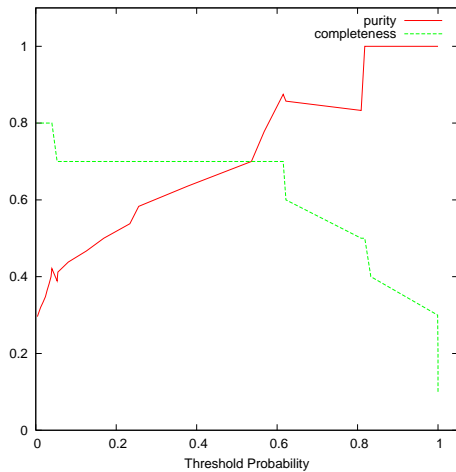


Figure 6. Purity and completeness as a function of the ‘threshold probability’ for the analysis of the simple simulated weak lensing data described in Section 3.2.

4 APPLICATION TO REALISTIC WEAK-LENSING SIMULATIONS

We now describe the results of our cluster finding algorithm when applied to simulated weak-lensing survey data derived from numerical N -body simulations.

4.1 Realistic weak-lensing survey simulation

In this case, the weak-lensing data is simulated using by ray-tracing through a numerical N -body simulation of structure formation (White (2005)), covering a 3×3 degree field of view. The cosmological model is taken to be a concordance Λ CDM model with parameters $\Omega_m = 0.3$, $\Omega_\Lambda = 0.8$, $\sigma_8 = 0.9$ and the Hubble parameter $h = 0.7$. The simulations employed 384^3 equal mass ($10^{10} M_\odot h^{-1}$) dark matter particles in a periodic cubical box of side $200 h^{-1} \text{Mpc}$ that was evolved to $z = 0$. The redshift distribu-

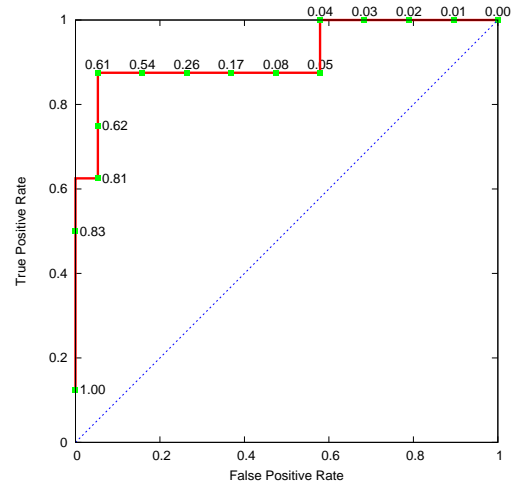


Figure 7. Receiver Operating Characteristic (ROC) curve obtained by varying the threshold probability p_{th} used in identifying candidate clusters for the analysis of the simple simulated weak lensing data-set discussed in Section 3.2. The points are labelled with their corresponding p_{th} value.

tion of the background galaxies was taken to be

$$p(z) \sim z^2 e^{-(z/z_0)^b}, \quad (30)$$

with $z_0 = 1.0$ and $b = 1.5$.

There are roughly 200 galaxies per arcmin² in the simulation, which represents the deepest space-based surveys. In practice, the signal-to-noise magnitude threshold gives around 100 galaxies per square arcminute and then insisting on knowing the photometric redshift of each galaxy pushes the number down to 40 – 70 per arcmin². Since there is no colour-magnitude information for the galaxies available in these simulations, we pick 65 galaxies per square arcminute randomly from the galaxy catalogue. The intrinsic ellipticity distribution of the galaxies is assumed to be Gaussian with $\sigma_{int} = 0.25$. We add Gaussian observational noise with standard deviation $\sigma_{obs} = 0.20$ to the sheared ellipticity of each galaxy.

Following Hennawi & Spergel (2005), we define all the halos with $M_{200} > 10^{13.5} h^{-1} M_\odot$ as candidates to be identified by weak-lensing, since the finite number of background galaxies and their intrinsic ellipticities places a lower limit on the mass of the halo that can be detected. The halo catalogue for the simulation, produced using the Friends-of-Friends algorithm (FoF) (Efsthathiou et al. 1985), contains 1368 halos with $10^{13.5} < M_{200}/h^{-1} M_\odot < 7.7 \times 10^{14}$ and $0 < z < 2.7$.

4.2 Analysis and results

Modelling the entire 3×3 degree² field of view represents a highly computationally expensive task and the MULTINEST algorithm would require a prohibitively large number of live points to be able to detect such a great many clusters. We therefore divide the data into 16 patches of 0.75×0.75 degree² each and use 4000 live points to analyse each patch. As before, we expand the ranges of uniform priors on the position of cluster centers to allow them to lie a little outside their respective patches, and we use uniform prior $\mathcal{U}(0, 15)$ for the concentration parameter. In order to determine the effect Press-Schechter mass function prior has on the detectability of clusters, as well as on the inferred cluster parameters, we perform the analysis using the joint Press-Schechter prior on M_{200}

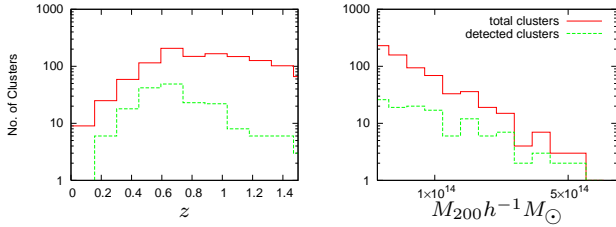


Figure 8. The total number of clusters in a given redshift and mass bin in the true catalogue (red) against the number of detected clusters (green) for the analysis with weak lensing simulation discussed in Section 4.1 with $p_{\text{th}} = 0.5$. The Press-Schechter mass function was used as a joint prior on M_{200} and z .

and z , as well as a logarithmic prior on M_{200} and uniform prior on z . In both cases, we assume the redshift range $0 < z \leq 4$ and the mass range $10^{13.5} < M_{200}/(h^{-1}M_{\odot}) \leq 5 \times 10^{15}$.

Before discussing the results from applying MULTINEST to the weak-lensing simulation, we note that the ‘true’ cluster catalogue for N -body simulation are, in fact, inferred using a halo finding algorithm. The FoF algorithm Efstathiou et al. (1985) is most often employed for this purpose and works by associating all the particles within a distance of one another that is some factor b of mean distance between the particles. The number of halos identified thus depends very strongly on the linking parameter b . Depending on the resolution of the N -body simulation and the value of b , FoF may or may not resolve out structures present within clusters. MULTINEST technique is very sensitive to any structure present within clusters and will classify these structures as individual clusters. Therefore, there is always a possibility of MULTINEST making an identification of two clusters very close to each other while the FoF algorithm would identified these as one cluster; this would result in a lower purity for the MULTINEST catalogue.

4.2.1 Completeness and purity

MULTINEST found around 600 halos out of which 293 and 268 halos were identified as candidate clusters using $p_{\text{th}} = 0.5$ with the Press-Schechter and log-uniform priors respectively. Catalogues matching was performed for each of these cluster candidates by finding the closest cluster in the true cluster catalogue for which all the cluster parameters lie within $4\text{-}\sigma$ of the inferred mean values. Any cluster candidate not having such a corresponding cluster in the true catalogue was identified as a *false positive*. Using this matching scheme, 187 and 175 cluster candidates were identified as *true positives*, giving a ‘purity’ 64% and 65%, for the Press-Schechter and log-uniform priors respectively. For the analysis with the Press-Schechter prior, we plot the number of clusters in the true catalogue and detected clusters as function of true cluster M_{200} and z in Figure 8. We plot purity and completeness as a function of cluster M_{200} and z in Figure 9. In Figure 10 we plot the completeness in the mass-redshift plane, for $M_{200} < 3 \times 10^{14}h^{-1}M_{\odot}$ and $z < 1.5$, since there are very few clusters in the true catalogue outside these ranges and consequently we suffer from small number statistics.

From Figures 9 and 10, it is clear that the completeness of our shear-selected cluster sample approaches unity only for massive clusters with $M_{200} \sim 5 \times 10^{14}h^{-1}M_{\odot}$. Hennawi & Spergel (2005) reached a similar conclusion using the Tomographic Matched Filtering (TMF) scheme. Unfortunately, a direct comparison with Hennawi & Spergel (2005) is not possible, as they used a

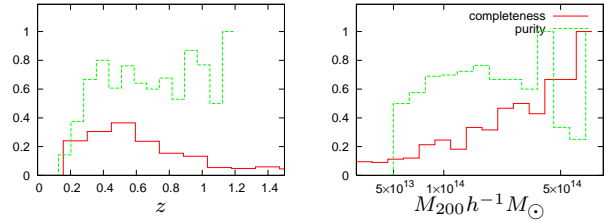


Figure 9. Completeness (red) and purity (green) for the analysis with weak lensing simulation discussed in Section 4.1 with $p_{\text{th}} = 0.5$. The Press-Schechter mass function was used as a joint prior on M_{200} and z .

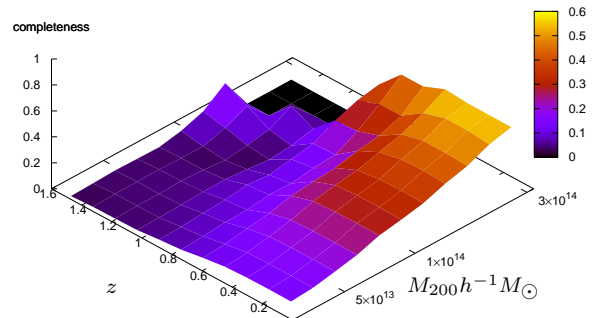


Figure 10. Completeness in mass-redshift plane for the analysis of the weak-lensing simulation discussed in Section 4.1 with $p_{\text{th}} = 0.5$. The Press-Schechter mass function was used as a joint prior on M_{200} and z .

different N -body simulation. Some other previous studies of shear-selected cluster samples White et al. (2002); Hamana et al. (2004) have also come to the same conclusion that they suffer from severe incompleteness except at the high-mass end.

In Figure 11 we plot completeness and purity as a function of threshold probability p_{th} for the analysis with the Press-Schechter prior. We notice that even for $p_{\text{th}} \sim 1$, purity is around 0.7, while one would expect it to be very close to unity. This discrepancy occurs because of the presence of sub-structure in high-mass clusters. As discussed in the previous section, the MULTINEST algorithm is very sensitive to any sub-structure within clusters, and identifies as separate clusters the halos that the FoF algorithm may or may not identify as belonging to a single cluster, depending on the impact parameter b .

4.2.2 Accuracy of parameter estimates

We now discuss the accuracy of recovered parameters of the detected clusters. The ‘true’ cluster catalogues did not have the concentration parameter and therefore we do not discuss the accuracy of inferred concentration of each cluster.

For $p_{\text{th}} = 0.5$, in Figures 12, 13 and 14, respectively, we plot for each detected cluster: the inferred cluster parameters against the true cluster parameters; the difference between the inferred parameters and the true parameters; and the difference between the inferred parameters and the true parameters against the true param-

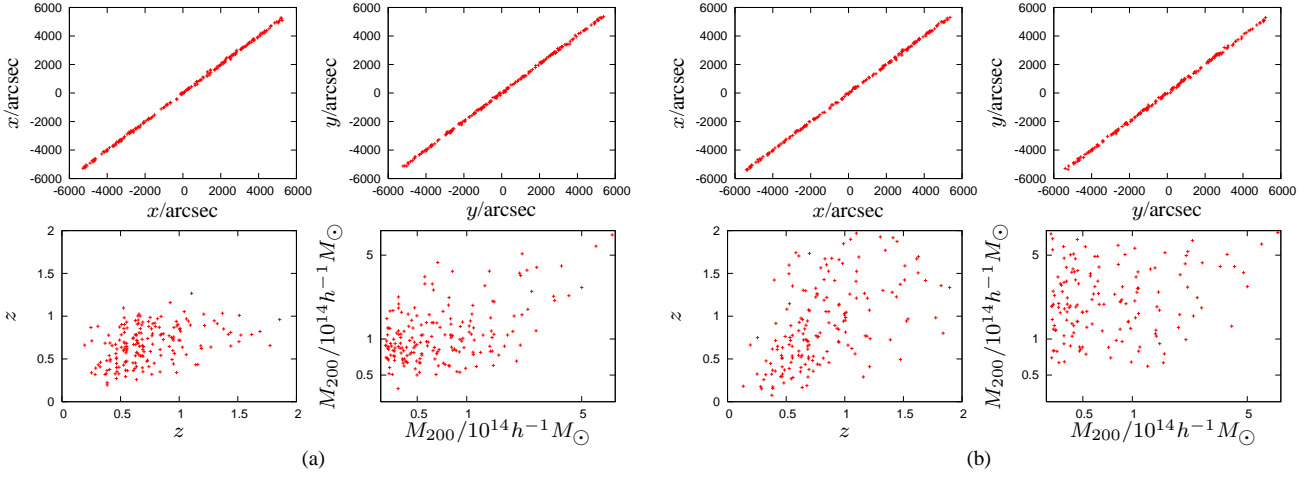


Figure 12. Inferred parameter values (on the y-axis) against the ‘true’ parameter values (on the x-axis) for each of the detected clusters. The analysis was performed with $p_{\text{th}} = 0.5$ using (a) the Press-Schechter mass function prior on M_{200} and z and (b) a logarithmic prior on M_{200} and uniform prior on z .

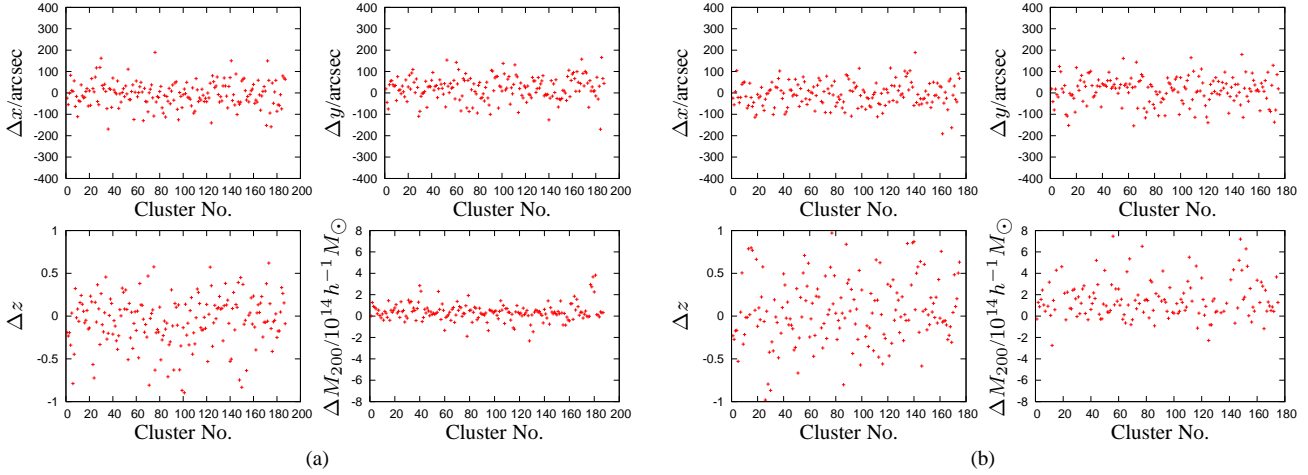


Figure 13. Difference between the inferred parameter values and the true parameter values from the cluster catalogue, plotted for each detected cluster. The analysis was performed with $p_{\text{th}} = 0.5$ using (a) the Press-Schechter mass function prior on M_{200} and z and (b) a logarithmic prior on M_{200} and uniform prior on z .

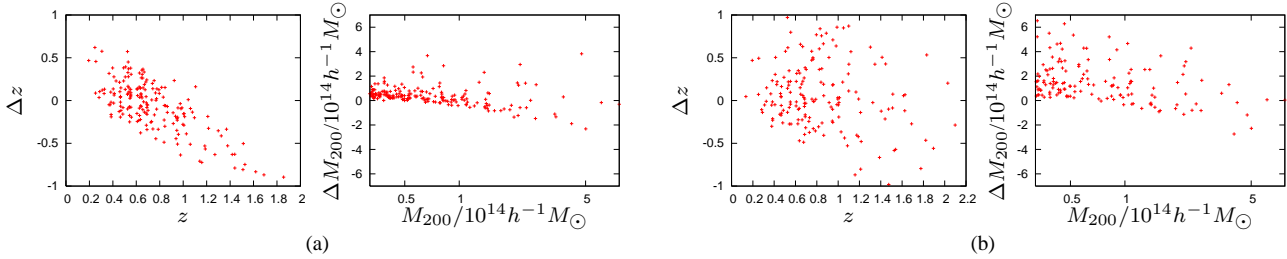


Figure 14. Difference between the inferred parameter values and the true parameter values from the cluster catalogue, plotted against the true parameter values for each of the detected clusters. The analysis was performed with $p_{\text{th}} = 0.5$ using (a) the Press-Schechter mass function prior on M_{200} and z and (b) a logarithmic prior on M_{200} and uniform prior on z .

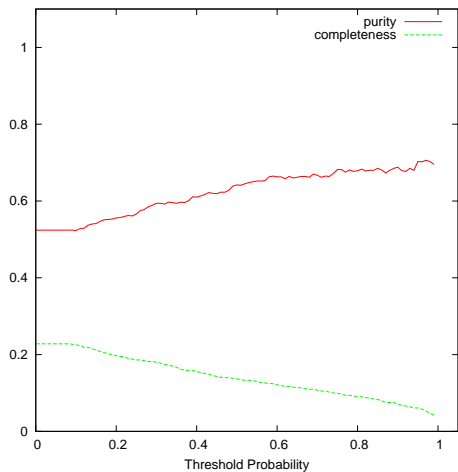


Figure 11. Purity and completeness as a function of the ‘threshold probability’ for the analysis of the simulated weak-lensing data described in Section 4.2. The Press-Schechter mass function was used as a joint prior on M_{200} and z .

eters. Each figure contains the results for the Press-Schechter and log-uniform priors.

It can be seen from these figures that the cluster positions have been reasonably well estimated, but the inferred cluster masses have generally been positively biased for both Press-Schechter and logarithmic priors on M_{200} . For logarithmic priors on M_{200} this bias is particularly strong. Applying the Press-Schechter prior does result in better parameter estimates for cluster masses but nevertheless, the inferred masses of the low-mass clusters have still been over-estimated. This result agrees well with what is already known from the N -body simulations, the Press-Schechter mass function over-estimates the abundance of high-mass clusters and under-estimates the abundance of low-mass clusters and consequently, the inferred masses of the low mass clusters have been over-estimated. This highlights the importance of having physically motivated priors for parameterising clusters in the weak lensing data-sets. This biasing of cluster masses, particularly at the low-mass end points to the fact that although the Press-Schechter mass function gives better estimates and reduces the bias in cluster parameters as compared with a logarithmic prior on M_{200} , it still does not fit this particular N -body simulation extremely well. The inferred cluster redshifts have a large scatter for both the Press-Schechter and logarithmic priors on M_{200} . This is because z is correlated with M_{200} and hence some additional information is required to break this degeneracy and get better estimates for both M_{200} and z .

We further note that we have assumed a spherical NFW model for the cluster mass profiles, while several studies have shown that the clusters are not necessarily spherical (see e.g. Shaw et al. 2006; Bett et al. 2007). Corless & King (2007, 2008) have recently shown that ignoring the triaxial 3D structure can result in inaccuracies in cluster parameter estimates. We plan to include the triaxial NFW mass profile in a future work to assess the importance of including 3D triaxial structure on cluster parameter estimation.

5 CONCLUSIONS

We have introduced a very efficient and robust approach to detecting galaxy clusters in wide-field weak lensing data-sets. This ap-

proach allows the parameterisation of each detected cluster. Furthermore, using Bayesian model selection, one can also calculate the probability odds for each detected cluster being ‘true’. This quantification of cluster detection allows flexibility in determining the cluster candidate selection criterion depending on the application. In spite of the non-linear nature of the analysis method, we are able to search at a rate of one-half square degree per hour on a single processor. The code is fully parallel, making this a viable technique even for the deepest weak-lensing surveys.

An application of our algorithm to simulated weak-lensing data derived by an N -body simulation showed that the shear-selected cluster sample suffers from severe incompleteness at the low-mass and high-redshift ends of the cluster distribution, with the completeness approaching unity only for massive clusters with $M_{200} \sim 5 \times 10^{14} h^{-1} M_{\odot}$. We also demonstrated the importance of the priors in estimating the masses and redshifts of low-mass clusters, since the lensing signal produced by them is particularly weak. We used the Press-Schechter mass function as a prior on cluster masses and redshift in this work and found it to produce inferred masses of the low-mass clusters that are biased low.

In a future study, we intend to extend this work by including the triaxial NFW mass profile to investigate what fraction of clusters show significant triaxiality in the Λ CDM model N -body simulation, and also to assess the importance of triaxiality in cluster parameter estimation.

ACKNOWLEDGEMENTS

This work was carried out largely on the Cambridge High Performance Computing Cluster Darwin and the authors would like to thank Dr. Stuart Rankin for computational assistance. FF is supported by the Cambridge Commonwealth Trust, Isaac Newton and the Pakistan Higher Education Commission Fellowships.

REFERENCES

- Allen S. W., Schmidt R. W., Fabian A. C., Ebeling H., 2003, MNRAS, 342, 287
- Bartelmann M., 1996, A&A, 313, 697
- Battye R. A., Weller J., 2003, Phys.Rev.D, 68, 083506
- Bett P., Eke V., Frenk C. S., Jenkins A., Helly J., Navarro J., 2007, MNRAS, 376, 215
- Bradač M., Lombardi M., Schneider P., 2004, A&A, 424, 13
- Bridle S.L., Hobson M.P., Lasenby A.N., Saunders R., 1999, MNRAS, 299, 895
- Corless V. L., King L. J., 2007, MNRAS, 380, 149
- Corless V. L., King L. J., 2008, ArXiv e-prints, 807
- Efstathiou G., Davis M., White S. D. M., Frenk C. S., 1985, ApJS, 57, 241
- Evrard A. E., MacFarland T. J., Couchman H. M. P., Colberg J. M., Yoshida N., White S. D. M., Jenkins A., Frenk C. S., Pearce F. R., Peacock J. A., Thomas P. A., 2002, ApJ, 573, 7
- Fawcett T., 2006, Pattern Recogn. Lett., 27, 861
- Feroz F., Hobson M. P., 2008, MNRAS, 384, 449
- Feroz F., Hobson M. P., Bridges M., 2008, MNRAS, submitted (arXiv0809.3437)
- Hamana T., Takada M., Yoshida N., 2004, MNRAS, 350, 893
- Hennawi J. F., Spergel D. N., 2005, ApJ, 624, 59
- Hobson M. P., McLachlan C., 2003, MNRAS, 338, 765
- Hoekstra H., Franx M., Kuijken K., 2000, ApJ, 532, 88

- Hoekstra H., Mellier Y., van Waerbeke L., Semboloni E., Fu L., Hudson M. J., Parker L. C., Tereno I., Benabed K., 2006, *ApJ*, 647, 116
- Jenkins A., Frenk C. S., White S. D. M., Colberg J. M., Cole S., Evrard A. E., Couchman H. M. P., Yoshida N., 2001, *MNRAS*, 321, 372
- Kaiser N., Squires G., 1993, *ApJ*, 404, 441
- Liddle A. R., 2007, *ArXiv Astrophysics e-prints*
- Marshall P., 2006, *MNRAS*, 372, 1289
- Marshall P. J., Hobson M. P., Gull S.F., Bridle S.L., 2002, *MNRAS*, 335, 1037
- Marshall P. J., Hobson M. P., Slosar A., 2003, *MNRAS*, 346, 489
- Massey R., Refregier A., Bacon D. J., Ellis R., Brown M. L., 2005, *MNRAS*, 359, 1277
- Massey R., Rhodes J., Ellis R., Scoville N., Leauthaud A., Finoguenov A., Capak P., Bacon D., Aussel H., Kneib J.-P., Koekemoer A., McCracken H., Mobasher B., 2007, *Nature*, 445, 286
- Meneghetti M., Bartelmann M., Moscardini L., 2003, *MNRAS*, 340, 105
- Navarro J. F., Frenk C. S., White S. D. M., 1997, *ApJ*, 490, 493
- Press W. H., Schechter P., 1974, *ApJ*, 187, 425
- Schneider P., King L., Erben T., 2000, *A&A*, 353, 41
- Schramm T., Kayser R., 1995, *A&A*, 299, 1
- Shaw L. D., Weller J., Ostriker J. P., Bode P., 2006, *ApJ*, 646, 815
- Sheth R. K., Mo H. J., Tormen G., 2001, *MNRAS*, 323, 1
- Skilling J., 2004, in Fischer R., Preuss R., Toussaint U. V., eds, *American Institute of Physics Conference Series Nested Sampling*, pp 395–405
- Squires G., Kaiser N., 1996, *ApJ*, 473, 65
- Starck J.-L., Pires S., Réfrégier A., 2006, *A&A*, 451, 1139
- Trotta R., 2007, *MNRAS*, 378, 72
- White M., 2005, *Astroparticle Physics*, 23, 349
- White M., van Waerbeke L., Mackey J., 2002, *ApJ*, 575, 640
- White S. D. M., Navarro J. F., Evrard A. E., Frenk C. S., 1993, *Nature*, 366, 429
- Wright C. O., Brainerd T. G., 2000, *ApJ*, 534, 34